

pubs.acs.org/JPCC Article

In Situ EXAFS-Based Nanothermometry of Heterodimer Nanocrystals under Induction Heating

Daniel J. Rosen, Shengsong Yang, Emanuele Marino, Zhiqiao Jiang, and Christopher B. Murray*



Cite This: https://doi.org/10.1021/acs.jpcc.2c00608



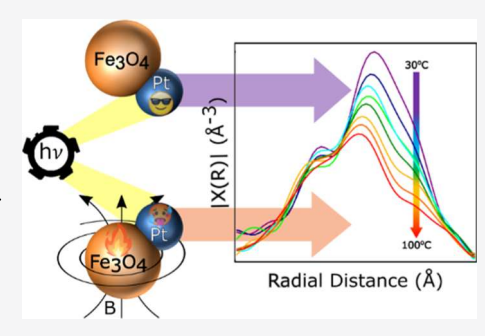
ACCESS

Metrics & More

Article Recommendations

Supporting Information

ABSTRACT: The ability to heat nanocrystalline materials through magnetic induction has been used in the fields of catalysis, biomedical sciences, and polymer degradation. However, the working temperature to which the inductively coupled material rises is still poorly understood. Herein, we use extended X-ray absorption fine structure spectroscopy in conjunction with thermal imaging to improve the understanding of heating in inductively coupled systems. After extraction of the Debye—Waller factor from the spectroscopy, we obtain the temperature of inductively heated nanocrystals from the correlated Debye model. We combine carbon-supported iron oxide nanocrystals as induction heating agents with platinum nanocrystals as thermal probes. By testing these nanocrystal species as both unattached nanocrystals and heterodimers, we report that nanostructured systems



show a significant temperature difference of up to 73.60 °C when compared to their local support environment. This result has implications for inductively heated catalysis, magnetic hyperthermia for targeted cell death, and polymer synthesis.

■ INTRODUCTION

Induction heating is the process of heating materials by exposure to high-frequency alternating current (AC) magnetic fields. For nearly 50 years, induction heating of nanocrystalline materials has been used in a range of fields, including inductive catalysis, ^{1–8} hyperthermia treatments for the death of cancer cells, ^{9–11} organic ¹² and solid-state ^{13,14} chemical reactions, and more recently, polymer sciences. ^{13,15} The emergence of induction heating as an alternative form of thermal excitation represents a valuable method to maintain the activity of a catalytic reaction while operating at reduced temperatures and pressures. ^{2–4,16} Additionally, using magnetically heated systems for polymer synthesis allows for the use of a magnetically separable catalyst ^{5,17} as a means to synthesize a useful product.

Nanocrystals (NCs) represent an important class of materials for catalysis 1-3,5-7,14,18 due to their large surfaceto-volume ratio. Pt and Pt alloy NCs are of particular interest as they show high levels of catalytic activity for a variety of electro-19-21 and thermo-22,23 catalytic reactions. Since Pt NCs are paramagnetic, their temperature is often regulated through radiant and conductive, herein called conventional, heating. However, these NCs may indirectly benefit from induction heating when in thermal contact with magnetic NCs, such as Fe₃O₄. Fe₃O₄ NCs are magnetic, resulting in induction heating due to magnetothermal hysteresis losses at ambient conditions. 7,9,16,24 Eddy currents also contribute to the amount of heating that the system will experience. 25-27 Due to the combination of these two mechanisms, accurately predicting magnetothermal losses experienced by the NCs during induction heating is a challenging problem. Therefore, experimental methods at the nanoscale must be developed to

improve our understanding of the thermal properties of NCs under induction heating.

Here, we design heterodimers, consisting of epitaxially attached Pt and Fe₃O₄ NCs, as a model system to demonstrate the efficacy of induction heating of catalytically relevant and paramagnetic species, such as Pt. 28-31 Fe₃O₄ NCs operate as a nanoscale inductive heat source, while Pt NCs remain nearly unaffected by the induction field and therefore act as a probe material for nanothermometry, while Fe₃O₄ has the potential to undergo phase transformations at higher temperatures and is therefore not directly measured. We design this combination of NC species to investigate the temperature difference of the NCs as compared to their local support environment. In the future, more advanced heterodimer systems could be studied such as PtCo-Fe₃O₄, Au-Fe₃O₄, or others. For this study, we choose conditions relevant to both thermo-2,4,16,22 and electro-20,23 catalysis, including a Vulcan XC-72R carbon support background, under N2, in the presence of 1-propanol, as described in the Materials and Methods section. Unraveling the relationship between induction heating and the working temperature of a material is crucial for the applications discussed previously. In catalysis, the temperature of the catalyst provides the thermal energy needed to overcome the

Received: January 25, 2022 Revised: January 29, 2022



activation barrier of the desired reaction. ^{1,3,4,32} Despite the importance of inductive heating of NCs, the understanding of the relationship between nanoscale induction heating and the final temperature remains poor, ^{1,10,13–15} with specific examples reported for iron alloys ^{2,3,16,33} and iron oxide. ^{11,12} This is especially true in studies that focus on the inductive heating of NCs. ^{1,9–11,34–49} Some studies report a uniform temperature distribution between NCs and their local support environment, ^{32–34,36,40,42,46,48,50–54} while others report a thermal difference between the two. ^{55–60} Many of the studies reporting a uniform temperature distribution come from experimental hyperthermia treatments ^{51–53} while those reporting a temperature difference come mainly from theory, especially with arguments for ballistic heat transfer at the nanoscale. ^{56–59,61}

To resolve this contention, we implement thermometry on the scale of several nanometers, or nanothermometry, to understand the thermal properties of NCs. 62,63 These techniques have been applied to a variety of materials from Au, 64,65 Pt, 66 rare earth elements, 67,68 and iron oxide. 1,10-12,33,47,49,69 Nanothermometry can be performed using temperature-dependent luminescence 70-75 or phosphorescence, 73,76-80 high-resolution thermal imaging, 81,82 and scanning thermal microscopy. 82 We implement in situ extended X-ray absorption fine structure (EXAFS) spectroscopy as a method of nanothermometry. Recent reports have shown that fitting the Debye-Waller factor extracted by EXAFS allows for the experimental determination of the temperature of the material under investigation. 29,62,64-66,83 In section S2, we show that the sensibility of an EXAFS-based nanothermometer is comparable to that of luminescent nanothermometers ^{84,85} and nearly 3 orders of magnitude higher than that of X-ray diffraction (XRD)-based nanothermometry methods. 33,84,85 The extraction of Debye—Waller factor is performed by fitting the spectroscopic data to the EXAFS equation (eq 1).

$$X(k) = \sum_{i} \frac{(N_{i}S_{0}^{2})f_{i}(k)}{kR_{i}^{2}} \sin(2kR_{i} + \delta_{i}(k))e^{-2\sigma_{i}^{2}k^{2}}e^{-2R_{i}/\lambda(k)}$$
(1)

In eq 1,^{29,65,86} X(k) is the scattering waveform at wavenumber k, N is the number of nearest-neighbor atoms, R is the distance to the nearest-neighbor atom, F_i is the scattering factor of the ith element, S_0 is a many-body amplitude reduction factor, δ is a phase shift, σ^2 is the Debye—Waller factor, and λ is the wavelength. We use this EXAFS-based nanothermometry to probe inductively heated NC systems and extract the temperature of the NCs. After extraction of the Debye—Waller factor from the temperature-dependent EXAFS, we use the correlated Debye model, seen in eq 2,^{86,87} without approximation, to determine the temperature of the inductively heated NCs and heterodimers.

$$\sigma_{\mathrm{T}}^{2} = \frac{3\hbar^{2}}{Mk_{\mathrm{B}}\theta_{\mathrm{D}}} \left[\frac{1}{4} + \left(\frac{T}{\theta_{\mathrm{D}}} \right)^{2} \int_{0}^{\theta_{\mathrm{D}}/T} \frac{x}{\mathrm{e}^{x} - 1} \mathrm{d}x \right]$$
(2)

In eq 2, M is the mass of the scattering atom, \hbar is Planck's constant, and $k_{\rm B}$ is Boltzmann's constant. The Debye temperature $(\theta_{\rm D})$ and the thermally dependent dynamic component of the Debye–Waller factor $(\sigma_{\rm T}^2)$ are also present in eq 2. The static component of the Debye–Waller factor, $\sigma_{\rm s}$, can be extracted through temperature-dependent EXAFS analysis. By simultaneously using EXAFS-based nanothermom-

etry and thermal imaging as nano- and macroscale thermometry, respectively, we demonstrate experimentally, for the first time, that a temperature difference exists between inductively heated NCs and their local support environment, with a maximum difference shown here to be 73.60 ± 14.50 °C at a magnetic field of H = 16.8 mT operating at 263 kHz.

MATERIALS AND METHODS

Materials. For this study, we used platinum(II) acetylacetonate [Pt(acac)₂, Sigma-Aldrich], iron (0) pentacarbonyl [Fe(CO)₅, Sigma-Aldrich], octadecene (ODE, 90%, Sigma-Aldrich), oleylamine (OLAm, 70%, Sigma-Aldrich), oleic acid (OAc, 90%, Sigma-Aldrich), hexane (reagent grade), isopropanol (IPA, reagent grade), nitrosonium tetrafluoroborate (NOBF₄, 97%, Acros Organics), and dimethyl formamide (DMF, 99%, Sigma-Aldrich).

NC Synthesis and Support Deposition. Pt NCs were synthesized via solvothermal methods. ²¹ Briefly, 0.5 mmol Pt(acac)₂ was combined with 10 mL of ODE, 0.5 mL of OLAm, and 0.5 mL of OAc in a 50 mL three-neck flask. The solution was degassed on a Schlenk line under 120 °C for 20 min. After switching to a N₂ atmosphere, the temperature was raised to 180 °C degrees, and 10 μ L of Fe(CO)₅ was injected swiftly. The reaction was maintained at 180 °C for another 1 h until it was cooled down to room temperature. The NCs were collected by centrifugation with the addition of IPA as the antisolvent and dispersed in 10 mL of hexane after synthesis. For the following growth to heterodimers, the Pt NCs were dispersed in 10 mL of ODE.

Pt–Fe₃O₄ heterodimers were synthesized through a modified procedure that is described by Hodges et al. ⁸⁸ In a 50 mL three-neck flask, 10 mL of ODE was combined with 1 mL of OLAm and 1 mL of OAc. The solution was degassed on a Schlenk line under 120 °C for 20 min. After switching to a N₂ atmosphere, 100 μ L of Fe(CO)₅ and 1 mL of Pt NC in the ODE solution mentioned above were injected swiftly, and the temperature was raised to 300 °C. The reaction was maintained at the targeted temperature for 1 h to allow the second growth. Finally, the heterodimers were transferred to centrifuge tubes and the addition of IPA caused the NCs to precipitate from the suspension. For Fe₃O₄ NCs, only the Fe(CO)₅ was injected as compared to both Pt NCs and Fe(CO)₅ for Pt–Fe₃O₄ heterodimers.

The NCs were then loaded on Vulcan XC-72R carbon at 10% of Pt, or for pure $\rm Fe_3O_4$ 10% of NC, by weight and combined under sonication for 1 h. 22,23,89 The NCs were collected by centrifugation. NOBF₄ was applied to remove the extra ligands on the surfaces of NCs as described by Dong et al. 90 The carbon-supported NCs were dispersed in 20 mL of ethanol, and 10 mL of 0.01 M NOBF₄ in DMF solution was added under sonication. After 10 min, the NCs on carbon were collected by centrifugation. The supernatant was then discarded, and extra NOBF₄ residue was washed using ethanol. The NCs on carbon were dried overnight at 70 °C under vacuum at 100 \pm 10 Torr.

NC Characterization. Transmission electron microscopy (TEM) was performed on a JEOL JEM-1400 microscope operating at 120 keV. High-resolution micrographs, scanning transmission electron micrographs, and energy-dispersive spectroscopy images were obtained using a JEOL F200 electron microscope with a cold-FEG emission source operated at 200 kV. The composition of the NCs was determined through inductively coupled plasma-optical

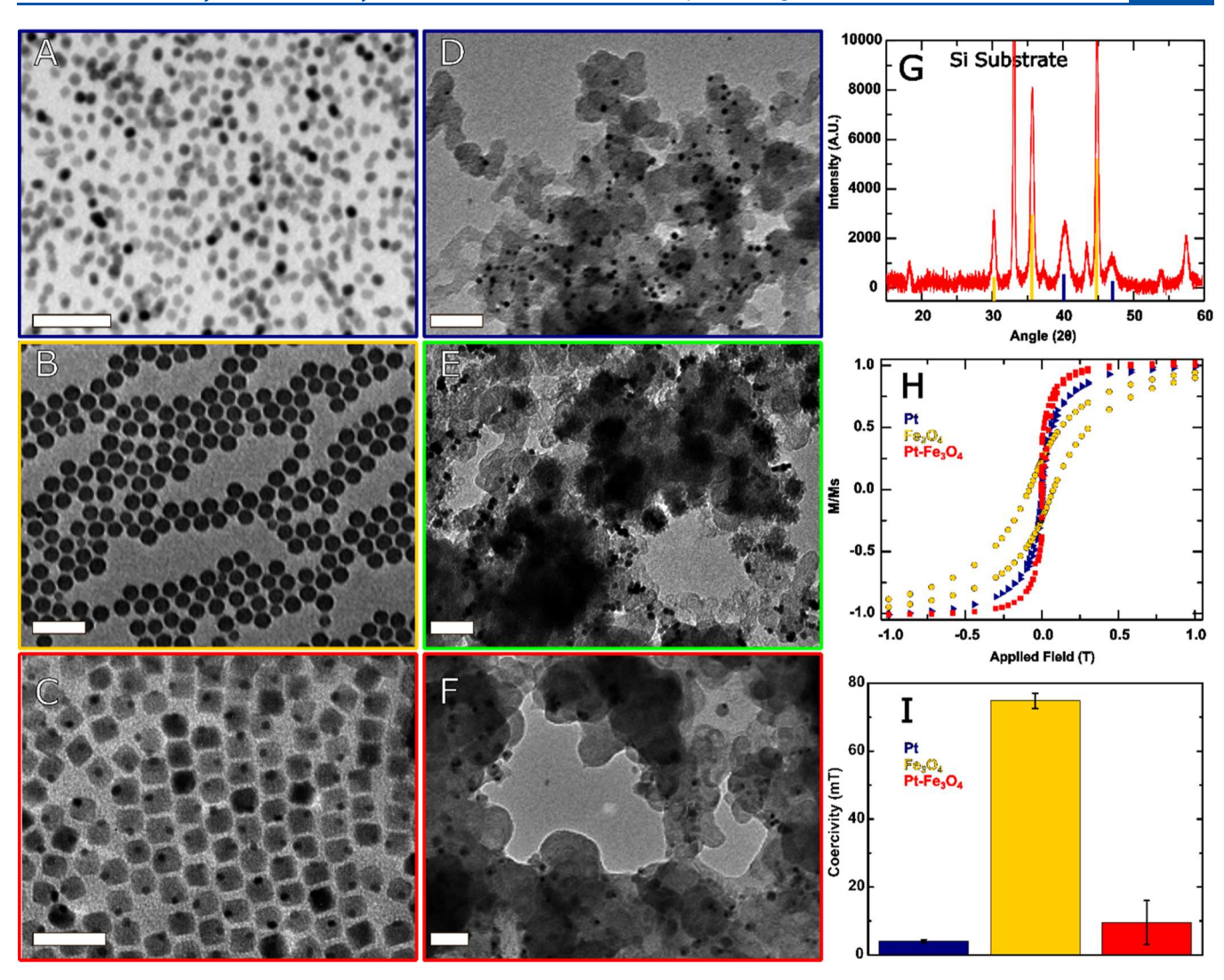


Figure 1. (A–C) shows TEM micrographs of as-synthesized Pt NCs, Fe₃O₄ NCs, and Pt–Fe₃O₄ heterodimers, respectively, while (D–F) shows Pt NCs, a physical mixture of Pt and Fe₃O₄ NCs, and Pt–Fe₃O₄ as deposited on carbon supports, respectively. Scale bars seen in the bottom left of each image are 50 nm. (G) shows XRD spectra for the heterodimer samples; blue indicates Pt peaks, while gold indicates Fe₃O₄. Reference XRD spectra are Pt–PCPDS: 70-2075 and Fe₃O₄–JCPDS: 00-003-0863. H shows magnetic hysteresis measurements, while I shows the obtained values of H_c .

emission spectrometry performed on a Spectro Genesis spectrometer with a concentric nebulizer. XRD was collected in the 2θ range of $15.0-60.0^{\circ}$ using a Rigaku SmartLab high-resolution diffractometer with Cu K α radiation ($\lambda=0.15416$ nm, 40 mA and 30 kV) at a resolution of 0.02° 2θ and a scan speed of 0.15 °/s. DC magnetic characterization was performed on a quantum design MPMS-XL7 superconductive quantum interference device magnetometer, and the sample hysteresis was measured at 15.0 K from 3.0×10^4 mT to -3.0×10^4 mT.

Thermal Characterization. Conventional thermal heating was performed using a custom sample cell in conjunction with a J-Kem Apollo temperature regulator. Heating cartridges were purchased from BriskHeat and operated at 120 V and between 75 and 300 W to allow for temperatures between 70.0 \pm 1.4 and 370.0 \pm 7.4 °C to be obtained. Inductive heating was performed using an Ambrell Easy Heat 1.2 kW induction heater with custom-turned water-cooled coils operating between the frequency range of 263 and 296 kHz, with exact frequency values for each power level given in Table S5. The induction sample holder was custom-designed and mounted

on a rotational stage. Thermal imaging was performed using a Fluke model TiS75 + thermal camera with an infrared resolution of 384 \times 288 pixels with a 40 \times 30° field of view; calibration allows for the thermal sensitivity of 40.0 mK and an accuracy of the greater value of either ± 2 °C or 2%. At 0.5 m focal distance from the sample, the spot size of the TiS75+ is 1.0 \times 1.0 mm. Each sample was loaded into polyimide tubing with an inner diameter equal to 2.77 mm and plugged with glass wool; subsequently, the samples were sealed under N_2 . Inductively heated samples were sealed in N_2 with the addition of 0.25 mL of 1-propanol to resemble typically flow catalytic reaction conditions more closely. $^{89,91-93}$

EXAFS Measurements. EXAFS was performed at the beamline for materials measurements (BMM), Beamline 6-BM at NSLS-II in the Brookhaven National Laboratory. Broadband X-rays were generated via a 3-pole wiggler source with energies ranging from 4.0 to 23.0 keV and a spot size of 300 μ m. A Si(111) monochromator was used with a resolution of 1.2 × 10^{-4} $\Delta E/E$ and a flux of 2 × 10^{12} at 10.0 keV. For Pt samples, the L₃ edge was used with E_0 equal to 11563.8 eV and a pseudo-channel-cut energy of 11868.6 eV. All data reported

here were taken in transmission mode at the Pt edge. The absorption data can be collected either in transmission or in fluorescence mode, or it can be collected for a reference foil. For the data we evaluate in this study, the absorption spectra were collected from the transmission chamber, besides the Pt foil reference, whose absorption was measured by the reference chamber. The reference Pt foil was used only in the determination of θ_{DN} and the basic EXAFS fitting parameters such as S_0^2 and the number of nearest neighbors. Data were analyzed using the Demeter software package. 94 Overall, fits to the data show a statistical significance of α < 0.04. Additional thermal images of the samples are shown in Figures S3 and S4, while the temperature values extracted from thermal imaging are reported in Table S4. The error bars for the EXAFS fittings were determined as described in Section S2 of the Supporting Information. The error could be decreased given additional repeated trials of data collection for each spectrum. For additional fitting data, see Figure S5.

Theoretical Modeling of Temperatures with EXAFS. After fitting the Debye—Waller factor values from the EXAFS equation (eq 1), previous literature reports show temperature dependence of the Debye—Waller factor through approximation methods, such as a first-order Taylor series method (eq 3). 29,65,86

$$\sigma_{\rm T}^2 \sim \frac{A}{\theta_{\rm D}} \left(\frac{1}{4} + \frac{T}{\theta_{\rm D}} \right)$$
 (3)

In eq 3, $\sigma_{\rm T}^2$ is the thermal component of the Debye–Waller factor, $\theta_{\rm D}$ is the Debye temperature, and A is a constant. In this report, we demonstrate, for the first time, a numerical method to obtain the temperature of NCs from the Debye–Waller factor directly using the correlated Debye model (eq 2)^{86,87} as a method of nanothermometry. The static component of the Debye–Waller factor, $\sigma_{\rm s}$, can be extracted through the temperature-dependent EXAFS analysis. Additionally, as $\theta_{\rm D}$ varies from bulk- to nano-scale materials, ⁸⁷ the $\theta_{\rm D}$ of the bulk material is altered to correspond to that of the nanomaterial based on eq 4. Equation 4 applies to any spherical NC and will reduce the material's $\theta_{\rm D}$. It is further changed based on experimentally determined thermal non-uniformities. ^{29,87}

$$\theta_{D_{\rm N}} = \theta_{D_{\rm b}} \left(1 - \frac{2D_{\rm atom}}{D_{\rm NC}} \right)^{1/2}$$
 (4)

In eq 4, the difference between the $\theta_{\rm D}$ of a bulk crystalline material versus that of a NC of spherical morphology is differentiated by the notation $\theta_{\rm Db}$ and $\theta_{\rm DN}$, respectively. $D_{\rm atom}$ is the diameter of the scattering atom, while $D_{\rm NC}$ is the average diameter of the NC being used, assuming a spherical geometry. This is the first EXAFS-based nanothermometry study to extract temperatures using the correlated Debye model without Taylor series or similar approximations. 1,33,65,66,69

■ RESULTS AND DISCUSSION

NC Characterization. Using the procedures described in the Materials and Methods section, 21,88,90 we synthesized 7.3 \pm 0.9 nm Pt, 18.3 \pm 0.6 nm Fe $_3$ O $_4$, and 18.5 \pm 1.0 nm Fe $_3$ O $_4$ components of the heterodimers (Pt–Fe $_3$ O $_4$) with Pt components equal in size to pure Pt NCs, as shown in Figure S1. The NCs are nearly monodisperse at approximately $\pm 5.0\%$ standard deviation, as shown by the TEM micrographs in

Figure 1A-C. Following their synthesis, the NCs were deposited on Vulcan carbon XC-72R supports at 10.0 wt % Pt loading, as shown by the TEM micrographs in Figure 1D-F. Figure 1G shows the existence of the Fe₃O₄ phase of iron oxide in the as-synthesized heterodimer samples before heating. Below the blocking temperature of 18.5 nm Fe₃O₄ NCs, approximately 250 K, 95 Fe₃O₄ NCs are superparamagnetic, as shown in Figure 1H. See Figure S9 for additional magnetic characterization. Superparamagnetic behavior is observed as the amount of applied magnetic field required to decrease the remnant magnetization to zero, or coercivity (H_c) of the material, is nonzero below the blocking temperature. 11,31,63 Provided that the magnetic field exceeds the $H_{\mathcal{O}}$ the amount of hysteresis losses contributing to the inductive heating is proportional to the H_c of the sample; otherwise, the heating will be proportional to the area of the hysteresis loop within the bounds of the applied magnetic field. 1,9–12,33,49,63,96,97 Consequently, Fe₃O₄ will undergo magnetothermal losses causing induction heating. 39-44,46 As Pt is paramagnetic and Fe₃O₄ is superparamagnetic, we choose Pt NCs to act as local thermal probes, while Fe₃O₄ NCs act as local heat sources. We measure the H_c of Pt and Fe₃O₄ NCs to be 4.0 and 74.8 mT, respectively, at 15.0 K. The hysteresis displayed at 15.0 K is representative of the magnetic properties of the NCs under high-frequency AC magnetic fields at room temperature as the phonons in the material are unable to couple rapidly to the field, thus mimicking conditions of a lower temperature; this phenomenon is often referred to as magnetic viscosity. 98,99 The H_c of Pt-Fe₃O₄ is lower than that of the iron oxide NCs, which is thought to be due to the epitaxially attached nature of the Pt and Fe $_3$ O $_4$ NCs. 24,96,97,100,101 This results in a Pt-Fe $_3$ O $_4$ H_c of 9.5 mT. The values of H_c are determined as the intercept of the hysteresis curve with zero magnetization.

To better show the morphology of the heterodimers, we perform high-resolution microscopy as shown in Figure 2A,B. Figure 2C,D additionally shows high-resolution micrographs of a physical mixture of Pt and Fe_3O_4 (Pt + Fe_3O_4) after deposition onto a Vulcan XC-72R carbon support material. In Figure 2A, Pt– Fe_3O_4 is shown at three different angles,

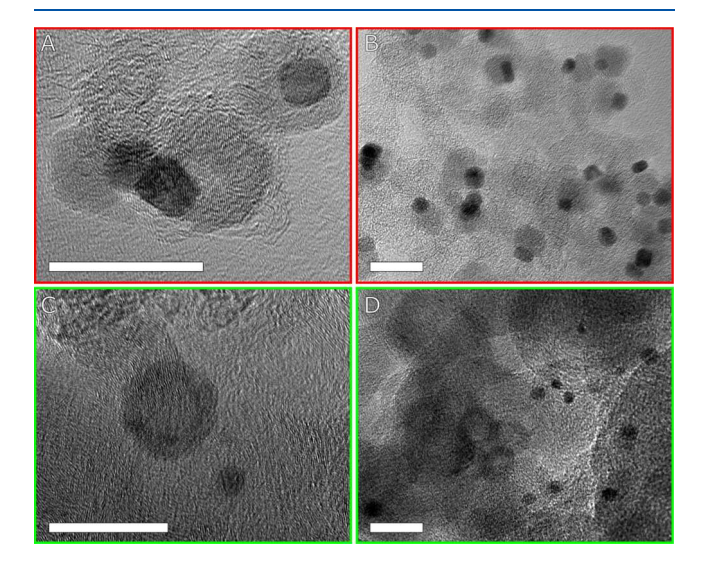


Figure 2. High-resolution TEM of (A,B) Pt– Fe_3O_4 and (C,D) Pt + Fe_3O_4 after the deposition of Vulcan XC-72R carbon supports. All scale bars are 20 nm.

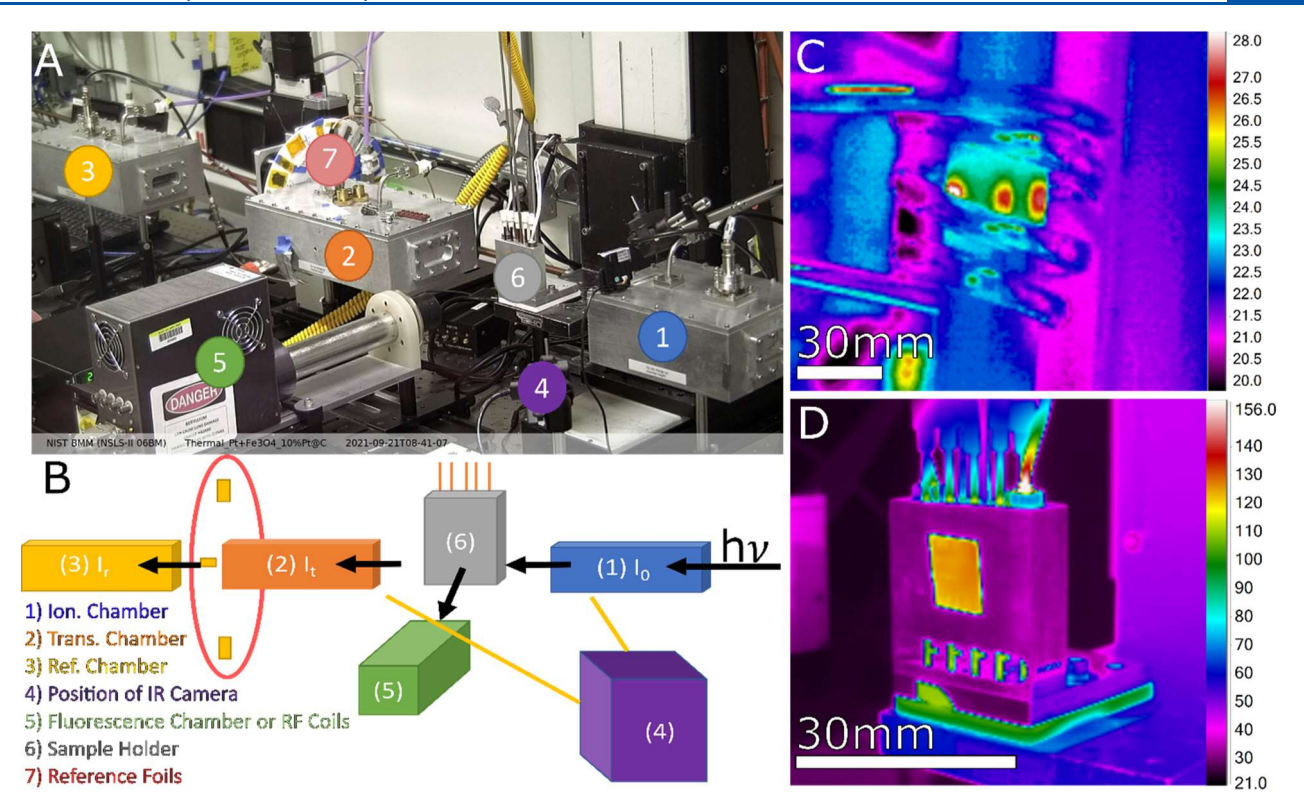


Figure 3. In (A), the experimental apparatus is seen, which corresponds to the schematic seen in (B). Arrows indicate X-ray direction. (C,D) shows examples of thermal imaging for inductively and conventionally heated samples, respectively. In (C), each hot spot in the center of the image is indicative of the sample location and temperature. All temperature scales are in Celsius.

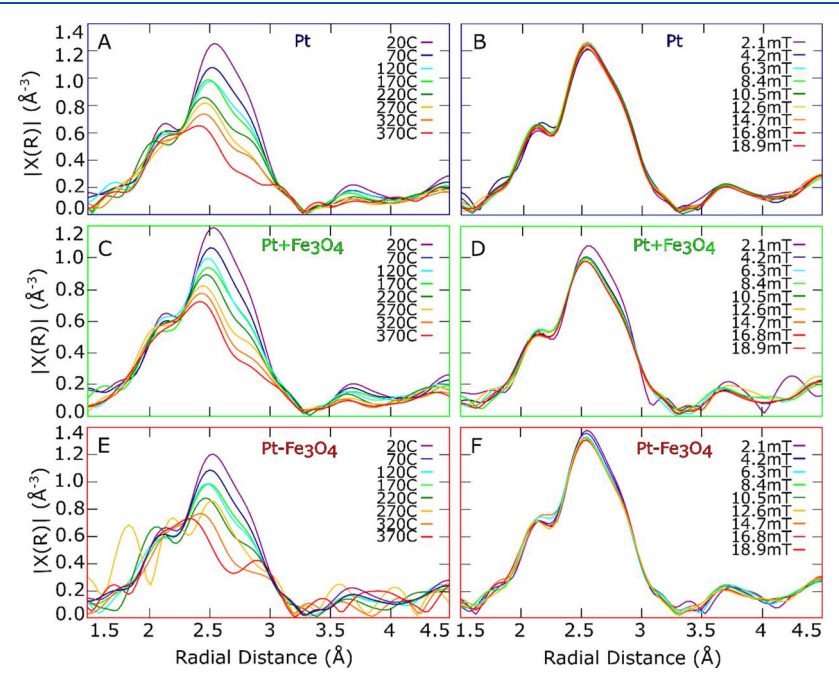


Figure 4. Real-space EXAFS data for (A,B) Pt (top/blue); (C,D) a physical mixture of Pt and Fe_3O_4 (Pt + Fe_3O_4 , middle/green); and (E,F) the heterodimer samples (Pt– Fe_3O_4 , bottom/red). Samples were either heated conventionally (A,C,E) or inductively (B,D,E).

demonstrating the epitaxially attached nature of the heterodimers. In Figure 2C, a single NC of both Pt and Fe_3O_4 is shown as representative of Pt + Fe_3O_4 . The smaller, higher-contrast species is Pt, while the other is Fe_3O_4 , as verified with energy-dispersive spectroscopy in Figure S12.

EXAFS Measurements. To perform in situ EXAFS, we used the experimental apparatus shown in Figure 3A–D.

All samples used in this study were taken in transmission mode or number 2 in Figure 3A,B. Figure 3C,D shows representative thermal images for both inductively heated samples and conventionally heated samples, respectively. In both cases, custom sample holders were used, as seen in Figure S2. For the inductive sample stage (Figure 3C), each thermal image contains data for three samples, and thermal imaging

was done for each EXAFS scan. In the case of the thermal stage shown in Figure 3D, the temperature of each sample is read directly from the images. Thermal imaging allows for the determination of the temperature of the local support environment, while temperature-dependent EXAFS allows for nanoscale temperature measurements.

We collected the nanothermometry EXAFS data on the Pt L-edge. To fit the data, we take a Fourier transform of the absorption spectra. The Fourier transform gives us a spectrum closely related to the radial distribution of atomic shells around the absorbing atom, in this case Pt. These real-space spectra allow us to probe the local atomistic structure of the absorbing species. Through observation of the real-space data, we can see general thermal trends under both conventional and inductive heating of the NCs, as seen in Figure 4A—F.

Increasing the temperature of the NCs results in increased disorder at the atomic level due to lattice vibrations, as captured by an increase in the Debye-Waller factor. As apparent from the EXAFS equation (eq 1), increasing the Debye-Waller factor causes a decrease in the peak intensity of the spectra while leaving the peak positions nearly unaffected. The conventionally heated samples of Pt, a physical mixture of unattached (independent) Pt + Fe₃O₄, and epitaxially attached Pt-Fe₃O₄ heterodimers confirm this general trend, as shown in the conventionally heated samples in Figure 4A,C,E, respectively. Additional changes in the EXAFS spectra appear when heating the heterodimers above 220 °C, as shown in Figure 4E, as well as peak shifts to lower radial distances at temperatures above room temperature. We attribute these features to compositional changes in the heterodimers, likely due to interdiffusion of the Pt and Fe₃O₄ components, therefore changing the overall atomic structure of the Pt atoms. $^{19,30,102-104}$ As we will show later, even at the highest Hin this study, 16.8 mT, the inductively heated samples only reach 108.85 ± 12.50 °C. Therefore, we do not expect the inductively heated samples to undergo any compositional changes.

For the inductively heated samples, the peak intensity of the Fourier transform of the absorption spectra decreases with increasing field in both Pt + Fe $_3$ O $_4$ NCs and Pt-Fe $_3$ O $_4$ heterodimers, as shown in Figure 4D,F, respectively, indicating an increase in temperature at higher levels of the magnetic field, above 14.7 mT. The only sample that does not show a trend with the applied field is the inductively heated Pt NC sample in Figure 4B; this is consistent with the paramagnetic character of Pt, as seen in Figure 1H. This can additionally be seen in the extracted Debye–Waller factors shown in this report.

Thermal Computation. We use the EXAFS data in conjunction with the correlated Debye model described in eq 3, ^{86,87} and the material parameters shown in Table S2, to determine the steady-state temperature reached by the inductively heated samples. Figure 5 shows that the average experimental results deviate systematically from the correlated Debye model.

As shown in eq 2, the Debye—Waller factor results from structural disorder, or atomic displacements, of both static and dynamic nature. Here, we are interested in the temperature-dependent dynamic component of the Debye—Waller factor. Therefore, to determine the temperature the NCs reach under induction heating, we first need to understand the static component from the experimentally obtained values of the Debye—Waller factor. In the absence of structural alteration,

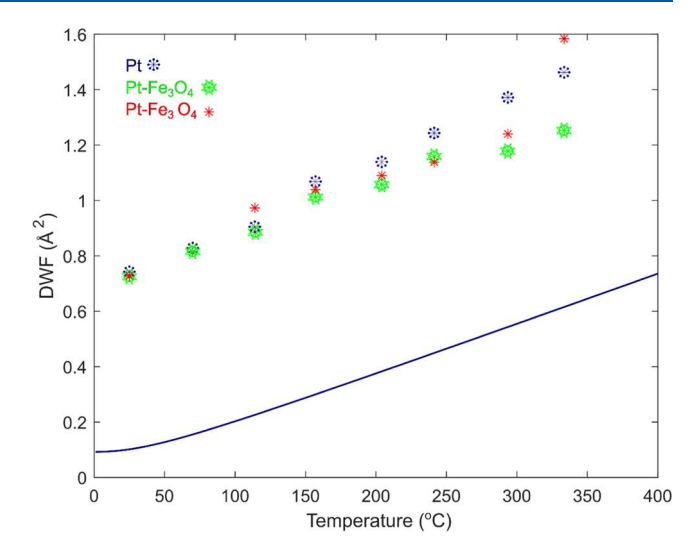


Figure 5. Correlated Debye model 86,87 for single-crystal Pt seen in the solid blue curve. Experimentally determined average values of the Debye—Waller factor for Pt, Pt + Fe₃O₄, and Pt—Fe₃O₄ are seen as symbols.

we expect the static component of the Debye-Waller factor to be independent of temperature. This is indeed the case here since based on the EXAFS analysis seen in Figure 4E, we have observed an onset for structural alteration in the heterodimers $^{19,102-104}$ only at temperatures higher than 220 $^{\circ}$ C, which is greater than the maximum temperature extracted from the induction heating of Pt-Fe₃O₄ at 16.8 mT, 108.85 ± 12.51 °C. As there is no structural alteration, we derived the value of the static disorder as the average difference between the Debye-Waller factor values obtained through fitting (symbols in F5) and through the correlated Debye model (line in F5). Values for the static disorder and a description of values determined for θ_D for each sample are shown in Table S3. Alternately, the static component can be determined by extrapolation of the experimental Debye-Waller factors to zero Kelvin, 105-107 as shown in Table S6. After removing the static disorder, the experimentally determined values of the Debye-Waller factor correlate to the theoretical values of the correlated Debye model^{86,87} at $R^2 = 0.995$, which is used to convert the Debye-Waller factor to a corresponding temperature, as shown in Figure 6A-D. Specifically, we use the corrected values of the Debye-Waller factor with known values of atomic mass, atomic diameter, and $\theta_{\rm D}$ to extract the temperature of the NCs from the correlated Debye model in eq 3^{29,86,87} using the MATLAB code provided in Section S3 of the Supporting Information.

By converting the temperatures from the Debye–Waller factor values in Figure 6A through the method established here, we demonstrate a correlation between the expected temperatures from conventional heating determined from thermal imaging and EXAFS-determined temperatures of 1.01 \pm 0.09 with an R^2 factor of 0.995, as shown in Figure 6B. This result highlights the reliability of our approach using EXAFS as a method of nanothermometry. As described in Section S2, the relative thermal sensitivity 84,85 (S_r) of our nanothermometer is found to be $3.58 \times 10^{-2} +/-6.71 \times 10^{-3}\%$ K⁻¹, this result is comparable to other lanthanide-based nanothermometers, 85 and it is 3 orders of magnitude higher than the sensitivity of XRD-based nanothermometers. For the inductively heated samples seen in Figure 6C,D, no difference is demonstrated for

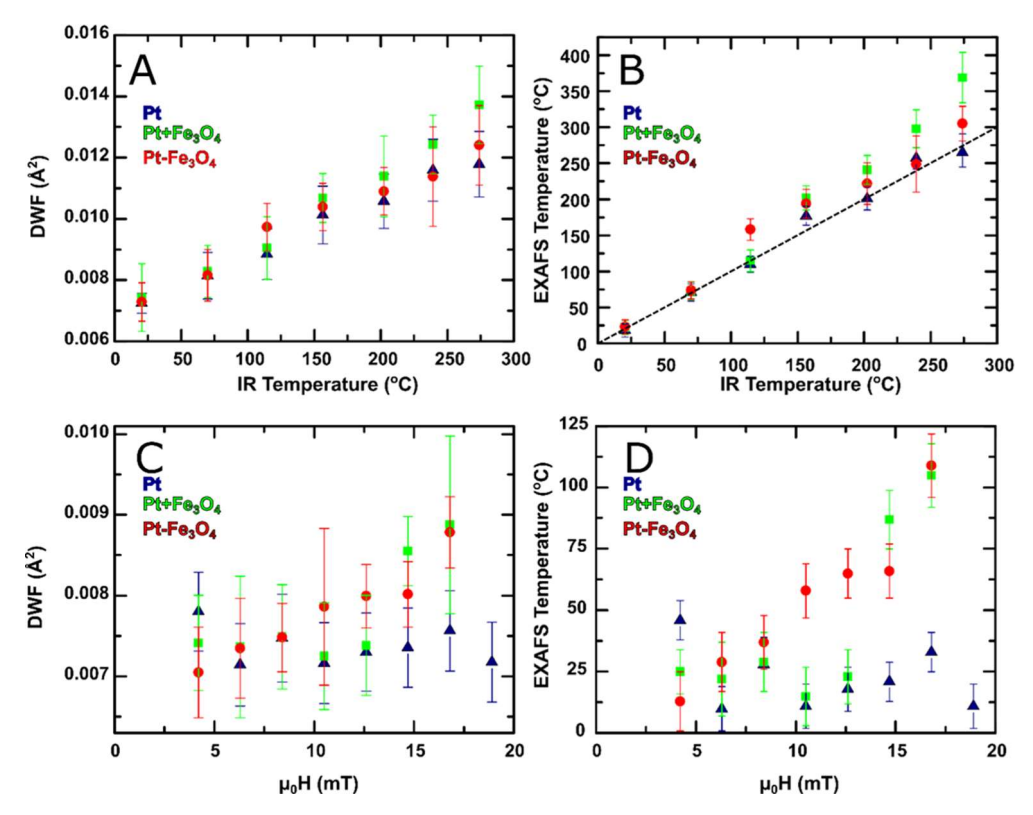


Figure 6. Thermally obtained results can be seen for (A) Debye–Waller factor values and (B) temperature values. In (B), the dashed line represents a 1–1 correspondence. Inductively heated results for the same can be seen in (C,D), respectively.

the pure Pt NCs, while the samples characterized by a positive value of H_c show heating especially at H greater than 14.7 mT.

By using the extracted values of temperature obtained through EXAFS, we can directly compare the temperature of the NCs to that of their local support environment. This comparison is shown in Figure 7.

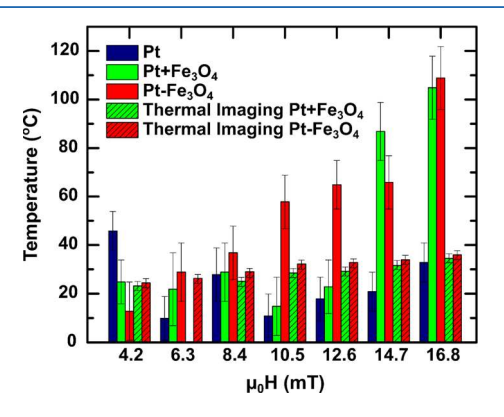


Figure 7. Description of temperatures reached through induction heating on both the scale of the NC, < 10 nm, and the macroscopic scale measured by thermal imaging, > 0.5 mm.

We observe the temperature of the local support environment through thermal imaging, as demonstrated in Figure 3C,D. The temperature of the local support environment is sensitive to the type of sample used, resulting in slightly different temperatures of the local support environment for Pt + $\rm Fe_3O_4$ and $\rm Pt{-}Fe_3O_4$ NC samples; however, these temperatures are statistically equivalent.

In contrast to a range of previous reports, 32,33,50-54 we show that induction heating results in a significant temperature difference between the NCs and their local support environment of up to 73.60 ± 14.50 °C. The measurement of a temperature difference between NCs and the support is observed for the Pt-Fe₃O₄ heterodimers at applied fields greater than 10.5 mT, which yields a difference of 28.50 ± 9.50 °C. It is also observable in the Pt + Fe₃O₄ at applied fields greater than 14.7 mT, which yields a difference of 55.25 ± 11.80 °C. After an initial onset of inductive heating at 14.7 mT, the temperature reached by the physical mixture, 86.85 ± 9.80 $^{\circ}$ C, matches that of the heterodimer samples, 75.85 \pm 7.25 $^{\circ}$ C, within the error bounds. We believe that the late onset of inductive heating for the physical mixture of magnetic and inert NCs is caused by thermal losses to the nearby support environment, which yields less thermal excitation of Pt as compared to samples with good thermal contact between Pt and Fe₃O₄. We see this trend again when observing a physical mixture of PtFe + Fe₃O₄ and heterodimer samples of PtFe and Fe₃O₄. As shown in Figure S8, these samples, which have similar compositions to the pure Pt \pm Fe₃O₄ samples²⁰ as seen in Table S1, demonstrate once again that we can achieve a temperature difference of up to 46.31 ± 9.54 °C at the H of 18.9 mT with the heterodimer samples, while the physical mixture displays no heating. We attribute the lack of heating once again to ballistic heat transfer^{57–59} between the Fe₃O₄ and the PtFe NCs in the PtFe + Fe₃O₄ samples.

For the highest H used in this study for the Pt + Fe₃O₄ NCs and Pt–Fe₃O₄ heterodimers, 16.8 mT, the Pt component of the samples reaches a temperature of 104.85 \pm 29.60 °C for Pt + Fe₃O₄ and 108.85 \pm 12.51 °C for Pt–Fe₃O₄. In contrast, the local support environment of Pt–Fe₃O₄ maintains a temperature of 35.25 \pm 2.00 °C, resulting in a temperature difference

of 73.60 \pm 14.50 °C between the heterodimers and their local support environment. This result has significant implications for hyperthermia treatment since the placement of inductively active NCs close to cancer cells may lead to their death more efficiently while preserving the surrounding healthy cells. ^{9,10,34,41,47,48,63,70} While the product of the applied field and frequency used in this study, which is approximately 6 \times 10¹⁰ A/m s, exceeds the maximum limit for safe exposure to humans, known as the Brezovich limit, it remains below the level seen in other studies, therefore maintaining clinical relevance through magnetic short pulse field exposure methods. ^{11,63} We additionally performed EXAFS-based nanothermometry under ambient conditions as seen in Figure S7, observing no changes compared to the samples measured under N₂ in the presence of 1-propanol.

We attribute the disagreement between our results, showing a thermal difference between the NCs and their local support environment and other reports demonstrating a uniform temperature distribution, ^{32,33,50-55} to the determination of the Debye-Waller factor through temperature-dependent EXAFS analysis in conjunction with the correlated Debye model. 86,87 Our approach allows for a significance of α < 0.04 and an accuracy in correlation of temperatures extracted from EXAFS and those extracted from the thermal imaging of 1.01 \pm 0.09 with R^2 = 0.995. In one example, the reporting of a uniform temperature distribution between NCs and their local support environment under induction heating may possibly be due to the use of supports embedded with Ni dopants at a non-negligible concentration in addition to NCs without good thermal contact. This likely results in an inductive-heatingbased increase of the support material and probe material, therefore decreasing the temperature difference between NCs and their local support environment. 33,108 Commonly, the temperature of the NCs under induction heating is determined through conventional calorimetry, ^{10,34,43,44,47,49,63} as seen in Figure S6. Calorimetry enables an accurate bulk determination of the intrinsic loss parameter (ILP), 43,47-49 allowing for the characterization of thermal loss under magnetic induction. However, the accuracy of this approach is limited by the measurement of the temperature of the bulk support environment, without considering the difference in temperature between the NCs and their local support environment. With only ILP values, it is difficult or nearly impossible to use these species in scenarios such as catalysis of thermally sensitive compounds or targeted cell death, where a thermal difference is a key aspect of the work. 9,18,48,63,70,109–111 Here, we have shown that the correlated Debye model can be used directly to calculate the temperature of the NCs, while the values of ILP can be used to extract the local support environment temperature. 47,48,86,87 Experimentally, the ILP of the local support environment was directly observed with a thermal imaging camera, and the thermal difference between the local support environment and the NCs was directly compared for complete thermal understanding of the system. Therefore, this study is not only the first to use in situ EXAFSbased nanothermometry to extract thermal measurements in inductively heated systems but also the first to jointly use temperature-dependent EXAFS and the unapproximated correlated Debye model for the determination of temperature.

CONCLUSIONS

We have demonstrated experimentally, for the first time, the presence of a temperature difference between heterodimers,

Pt-Fe₃O₄, and their local support environment of up to 73.60 \pm 14.50 °C. To show this, we used temperature-dependent EXAFS spectroscopy in conjunction with thermal imaging to allow for nanothermometry and macroscopic scale thermometry, respectively. The ability to determine the temperature differences observed in this study represents a capability enabled by in situ EXAFS-based nanothermometry. The determination of a temperature difference has implications in inductive catalysis, 1-8 hyperthermia treatments for the death of cancer cells, 9-11 and polymer sciences. 13,15 In catalysis, the ability to determine the temperature difference between the NCs and their support material under induction heating is a key step toward performing catalytic reactions on stabilitylimited reactants. Performing catalysis at room temperature without external heat sources, termed "cold catalysis", 33 is enabled through the thermal understanding of induction heating. 18,33,109-111 Using NCs as localized sources of heat through induction paves the way to performing low-temperature reactions without compromising on activity and presents a valuable area of research to explore. The observation of a temperature difference between NCs and the local support environment of up to 73.60 °C significantly improves our thermal understanding of inductive heating in NCs and is a necessary step toward applications in cold catalysis.

ASSOCIATED CONTENT

Supporting Information

The Supporting Information is available free of charge at https://pubs.acs.org/doi/10.1021/acs.jpcc.2c00608.

Additional NC characterization, sample holder designs, example IR imaging and temperatures, example fitting data, calorimetry, EXAFS spectra of ambient induction heating, EXAFS temperature of PtFe alloys, calculation parameters, values of the static Debye—Waller factor, frequency of magnetic field, description of error calculation, and code used for correlated Debye model analysis (PDF)

AUTHOR INFORMATION

Corresponding Author

Christopher B. Murray — Materials Science and Engineering and Chemistry Department, University of Pennsylvania, Philadelphia, Pennsylvania 19104, United States; Email: cbmurray@sas.upenn.edu

Authors

Daniel J. Rosen — Materials Science and Engineering, University of Pennsylvania, Philadelphia, Pennsylvania 19104, United States; oorcid.org/0000-0003-1463-7363

Shengsong Yang — Chemistry Department, University of Pennsylvania, Philadelphia, Pennsylvania 19104, United States; orcid.org/0000-0002-1386-7549

Emanuele Marino — Chemistry Department, University of Pennsylvania, Philadelphia, Pennsylvania 19104, United States

Zhiqiao Jiang – Materials Science and Engineering and Chemistry Department, University of Pennsylvania, Philadelphia, Pennsylvania 19104, United States

Complete contact information is available at: https://pubs.acs.org/10.1021/acs.jpcc.2c00608

Author Contributions

D.J.R. and S.Y. contributed equally. D.J.R. and S.Y. performed the EXAFS characterization and analysis. D.J.R. led the beamline study. S.Y. synthesized the NCs. E.M. performed theoretical calculations. Z.J. assisted with the analysis of theoretical data. C.B.M. supervised the work. All authors contributed to writing and editing the manuscript.

Notes

The authors declare no competing financial interest.

ACKNOWLEDGMENTS

D.J.R., S.Y., and C.B.M. acknowledge primary support from the Catalysis Center for Energy Innovation, an Energy Frontier Research Center funded by the U.S. Department of Energy, Office of Science, Office of Basic Energy Sciences under Award no. DE-SC0001004. E.M. and C.B.M. acknowledge support from the Office of Naval Research Multidisciplinary University Research Initiative Award ONR N00014-18-1-2497. D.J.R. acknowledges support from the Vagelos Institute for Energy Science and Technology Fellowship Program. Z.J. acknowledges support from the Vagelos Integrated Program in Energy Research. C.B.M. acknowledges the Richard Perry University Professorship at the University of Pennsylvania. This research used the BMM (6-BM) of the National Synchrotron Light Source II, a U.S. Department of Energy (DOE) Office of Science User Facility operated for the DOE Office of Science by Brookhaven National Laboratory under contract no. DE-SC0012704. We would like to thank NIST, BNL, DOC, and DOE staff for all of their help and support and especially B. Ravel for his contribution to the spectroscopy and analysis used in this work. This work was carried out in part at the Singh Center for Nanotechnology, which is supported by the NSF National Nanotechnology Coordinated Infrastructure Program under grant NNCI-2025608.

REFERENCES

- (1) Wang, W.; Tuci, G.; Duong-Viet, C.; Liu, Y.; Rossin, A.; Luconi, L.; Nhut, J.-M.; Nguyen-Dinh, L.; Pham-Huu, C.; Giambastiani, G. Induction Heating: An Enabling Technology for the Heat Management in Catalytic Processes. *ACS Catal.* **2019**, *9*, 7921–7935.
- (2) Marin, I. M.; De Masi, D.; Lacroix, L.-M.; Fazzini, P.-F.; van Leeuwen, P. W. N. M.; Asensio, J. M.; Chaudret, B. Hydrodeoxygenation and Hydrogenolysis of Biomass-Based Materials Using FeNi Catalysts and Magnetic Induction. *Green Chem.* **2021**, 23, 2025–2036.
- (3) Marbaix, J.; Mille, N.; Lacroix, L.-M.; Asensio, J. M.; Fazzini, P.-F.; Soulantica, K.; Carrey, J.; Chaudret, B. Tuning the Composition of FeCo Nanoparticle Heating Agents for Magnetically Induced Catalysis. ACS Appl. Nano Mater. 2020, 3, 3767–3778.
- (4) Asensio, J. M.; Miguel, A. B.; Fazzini, P. F.; van Leeuwen, P. W. N. M.; Chaudret, B.B. . Hydrodeoxygenation Using Magnetic Induction :High -TemperatureHeterogeneous Catalysis in Solution. *Angew. Chem., Int. Ed.* **2019**, *58*, 11306–11310.
- (5) Shokouhimehr, M. Magnetically Separable and Sustainable Nanostructured Catalysts for Heterogeneous Reduction of Nitroaromatics. *Catalysts* **2015**, *5*, 534–560.
- (6) Vinum, M. G.; Almind, M. R.; Engbæk, J. S.; Vendelbo, S. B.; Hansen, M. F.; Frandsen, C.; Bendix, J.; Mortensen, P. M. Dual-Function Cobalt—Nickel Nanoparticles Tailored for High-Temperature Induction-Heated Steam Methane Reforming. *Angew. Chem., Int. Ed.* **2018**, *57*, 10569—10573.
- (7) Gyergyek, S.; Kocjan, A.; Grilc, M.; Likozar, B.; Hočevar, B.; Makovec, D. A Hierarchical Ru-Bearing Alumina/Magnetic Iron-Oxide Composite for the Magnetically Heated Hydrogenation of Furfural. *Green Chem.* **2020**, *22*, 5978–5983.

- (8) Díaz-Puerto, Z. J.; Raya-Barón, Á.; van Leeuwen, P. W. N. M.; Asensio, J. M.; Chaudret, B. Determination of the Surface Temperature of Magnetically Heated Nanoparticles Using a Catalytic Approach. *Nanoscale* **2021**, *13*, 12438–12442.
- (9) Hoopes, P. J.; Strawbridge, R. R.; Gibson, U. J.; Zeng, Q.; Pierce, Z. E.; Savellano, M.; Tate, J. A.; Ogden, J. A.; Baker, I.; Ivkov, R.; et al. Intratumoral Iron Oxide Nanoparticle Hyperthermia and Radiation Cancer Treatment. *Proc. SPIE-Int. Soc. Opt. Eng.* **2007**, *6440*, 64400K.
- (10) Moroz, P.; Jones, S. K.; Gray, B. N. Magnetically Mediated Hyperthermia: Current Status and Future Directions. *Int. J. Hyperther.* **2002**, *18*, 267–284.
- (11) Lee, J.-H.; Kim, B.; Kim, Y.; Kim, S.-K. Ultra-High Rate of Temperature Increment from Superparamagnetic Nanoparticles for Highly Efficient Hyperthermia. *Sci. Rep.* **2021**, *11*, 1–9.
- (12) Hubbard, J. W.; Orange, F.; Guinel, M. J.-F.; Guenthner, A. J.; Mabry, J. M.; Sahagun, C. M.; Rinaldi, C. Curing of a Bisphenol E Based Cyanate Ester Using Magnetic Nanoparticles as an Internal Heat Source through Induction Heating. *ACS Appl. Mater. Interfaces* **2013**, *5*, 11329—11335.
- (13) Marques, F. D.; de Souza, M. N.; de Souza, F. G. Sealing System Activated by Magnetic Induction Polymerization. *J. Appl. Polym. Sci.* **2017**, *134*, 45549.
- (14) Zimmerer, C.; Mejia, C.; Utech, T.; Arnhold, K.; Janke, A.; Wosnitza, J. Inductive Heating Using a High-Magnetic-Field Pulse to Initiate Chemical Reactions to Generate Composite Materials. *Polymers* **2019**, *11*, 535.
- (15) Rahimi, A.; García, J. M. Chemical Recycling of Waste Plastics for New Materials Production. *Nat. Rev. Chem.* **2017**, *1*, 1–11.
- (16) De Masi, D.; Asensio, J. M.; Fazzini, P. F.; Lacroix, L. M.; Chaudret, B. Engineering Iron—Nickel Nanoparticles for Magnetically Induced CO2 Methanation in Continuous Flow. *Angew. Chem., Int. Ed.* **2020**, *59*, 6187–6191.
- (17) Shylesh, S.; Schünemann, V.; Thiel, W. R. Magnetically Separable Nanocatalysts: Bridges between Homogeneous and Heterogeneous Catalysis. *Angew. Chem., Int. Ed.* **2010**, *49*, 3428—3459.
- (18) Asensio, J. M.; Marbaix, J.; Mille, N.; Lacroix, L.-M.; Soulantica, K.; Fazzini, P.-F.; Carrey, J.; Chaudret, B. To Heat or Not to Heat: A Study of the Performances of Iron Carbide Nanoparticles in Magnetic Heating. *Nanoscale* **2019**, *11*, 5402–5411.
- (19) Zhang, P.; Li, R.; Huang, Y.; Chen, Q. A Novel Approach for the in Situ Synthesis of Pt–Pd Nanoalloys Supported on Fe3O4@C Core–Shell Nanoparticles with Enhanced Catalytic Activity for Reduction Reactions. ACS Appl. Mater. Interfaces 2014, 6, 2671–2678
- (20) Zhang, S.; Hao, Y.; Su, D.; Doan-Nguyen, V. V. T.; Wu, Y.; Li, J.; Sun, S.; Murray, C. B. Monodisperse Core/Shell Ni/FePt Nanoparticles and Their Conversion to Ni/Pt to Catalyze Oxygen Reduction. *J. Am. Chem. Soc.* **2014**, *136*, 15921–15924.
- (21) Kang, Y.; Li, M.; Cai, Y.; Cargnello, M.; Diaz, R. E.; Gordon, T. R.; Wieder, N. L.; Adzic, R. R.; Gorte, R. J.; Stach, E. A.; Murray, C. B. Heterogeneous Catalysts Need Not Be so "Heterogeneous": Monodisperse Pt Nanocrystals by Combining Shape-Controlled Synthesis and Purification by Colloidal Recrystallization. *J. Am. Chem. Soc.* **2013**, *135*, 2741–2747.
- (22) Luo, J.; Lee, J. D.; Yun, H.; Wang, C.; Monai, M.; Murray, C. B.; Fornasiero, P.; Gorte, R. J. Base Metal-Pt Alloys: A General Route to High Selectivity and Stability in the Production of Biofuels from HMF. *Appl. Catal. B Environ.* **2016**, *199*, 439–446.
- (23) Lee, J. D.; Jishkariani, D.; Zhao, Y.; Najmr, S.; Rosen, D.; Kikkawa, J. M.; Stach, E. A.; Murray, C. B. Tuning the Electrocatalytic Oxygen Reduction Reaction Activity of Pt—Co Nanocrystals by Cobalt Concentration with Atomic-Scale Understanding. ACS Appl. Mater. Interfaces 2019, 11, 26789—26797.
- (24) Morales, I.; Costo, R.; Mille, N.; da Silva, G.; Carrey, J.; Hernando, A.; de la Presa, P. High Frequency Hysteresis Losses on γ -Fe2O3 and Fe3O4: Susceptibility as a Magnetic Stamp for Chain Formation. *Nanomaterials* **2018**. *8*. 970.

- (25) Jiang, Y. Z.; Tan, Y.; Gao, Z.; Nakamura, K.; Liu, W. B.; Wang, S. Z.; Zhong, H.; Wang, B. B. Determination of Eddy Current Response with Magnetic Measurements. *Rev. Sci. Instrum.* **2017**, *88*, 093510.
- (26) Davis, L. C.; Reitz, J. R. Eddy Currents in Finite Conducting Sheets. J. Appl. Phys. 1971, 42, 4119.
- (27) García-Martín, J.; Gómez-Gil, J.; Vázquez-Sánchez, E. Non-Destructive Techniques Based on Eddy Current Testing. *Sensors* **2011**, *11*, 2525.
- (28) Geninatti, T.; Bruno, G.; Barile, B.; Hood, R. L.; Farina, M.; Schmulen, J.; Canavese, G.; Grattoni, A. Impedance Characterization, Degradation, and in Vitro Biocompatibility for Platinum Electrodes on BioMEMS. *Biomed. Microdevices* **2015**, *17*, 1–11.
- (29) Duc, N. B.; Tho, V. Q.; Tien, T. S.; Khoa, D. Q.; Hieu, H. K. Pressure and Temperature Dependence of EXAFS Debye-Waller Factor of Platinum. *Radiat. Phys. Chem.* **2018**, *149*, 61–64.
- (30) Rong, C.-b.; Nandwana, V.; Poudyal, N.; Li, Y.; Liu, J. P.; Ding, Y.; Wang, Z. L. Formation of Fe3Pt Phase in FePt-Based Nanocomposite Magnets. J. Phys. D: Appl. Phys. 2007, 40, 712.
- (31) Bean, C. P.; Livingston, J. D. Superparamagnetism. *J. Appl. Phys.* **1959**, *30*, S120.
- (32) Martínez-Prieto, L. M.; Marbaix, J.; Asensio, J. M.; Cerezo-Navarrete, C.; Fazzini, P.-F.; Soulantica, K.; Chaudret, B.; Corma, A. Ultrastable Magnetic Nanoparticles Encapsulated in Carbon for Magnetically Induced Catalysis. *ACS Appl. Nano Mater.* **2020**, 3, 7076–7087.
- (33) Faure, S.; Mille, N.; Kale, S. S.; Asensio, J. M.; Marbaix, J.; Farger, P.; Stoian, D.; van Beek, W.; Fazzini, P.-F.; Soulantica, K.; et al. Internal Temperature Measurements by X-Ray Diffraction on Magnetic Nanoparticles Heated by a High-Frequency Magnetic Field. *J. Phys. Chem. C* **2020**, *124*, 22259–22265.
- (34) Deatsch, A. E.; Evans, B. A. Heating Efficiency in Magnetic Nanoparticle Hyperthermia. *J. Magn. Magn. Mater.* **2014**, 354, 163–172.
- (35) Hergt, R.; Dutz, S.; Röder, M. Effects of Size Distribution on Hysteresis Losses of Magnetic Nanoparticles for Hyperthermia. *J. Phys.: Condens. Matter* **2008**, 20, 385214.
- (36) Mohapatra, J.; Nigam, S.; Gupta, J.; Mitra, A.; Aslam, M.; Bahadur, D. Enhancement of Magnetic Heating Efficiency in Size Controlled MFe 2 O 4 (M = Mn, Fe, Co and Ni) Nanoassemblies. *RSC Adv.* **2015**, 5, 14311–14321.
- (37) Papaefthymiou, G. C. Nanoparticle Magnetism. *Nano Today* **2009**, *4*, 438–447.
- (38) de la Presa, P.; Luengo, Y.; Multigner, M.; Costo, R.; Morales, M. P.; Rivero, G.; Hernando, A. Study of Heating Efficiency as a Function of Concentration, Size, and Applied Field in γ -Fe2O3 Nanoparticles. *J. Phys. Chem. C* **2012**, *116*, 25602–25610.
- (39) Levy, M.; Quarta, A.; Espinosa, A.; Figuerola, A.; Wilhelm, C.; García-Hernández, M.; Genovese, A.; Falqui, A.; Alloyeau, D.; Buonsanti, R.; et al. Correlating Magneto-Structural Properties to Hyperthermia Performance of Highly Monodisperse Iron Oxide Nanoparticles Prepared by a Seeded-Growth Route. *Chem. Mater.* **2011**, 23, 4170–4180.
- (40) Ruta, S.; Chantrell, R.; Hovorka, O. Unified Model of Hyperthermia via Hysteresis Heating in Systems of Interacting Magnetic Nanoparticles. *Sci. Rep.* **2015**, *5*, 1–7.
- (41) Nikitin, A.; Khramtsov, M.; Garanina, A.; Mogilnikov, P.; Sviridenkova, N.; Shchetinin, I.; Savchenko, A.; Abakumov, M.; Majouga, A. Synthesis of Iron Oxide Nanorods for Enhanced Magnetic Hyperthermia. *J. Magn. Magn. Mater.* **2019**, *469*, 443–449.
- (42) Nemati, Z.; Alonso, J.; Rodrigo, I.; Das, R.; Garaio, E.; García, J. Á.; Orue, I.; Phan, M.-H.; Srikanth, H. Improving the Heating Efficiency of Iron Oxide Nanoparticles by Tuning Their Shape and Size. *J. Phys. Chem. C* **2018**, *122*, 2367–2381.
- (43) He, S.; Zhang, H.; Liu, Y.; Sun, F.; Yu, X.; Li, X.; Zhang, L.; Wang, L.; Mao, K.; Wang, G.; et al. Maximizing Specific Loss Power for Magnetic Hyperthermia by Hard—Soft Mixed Ferrites. *Small* **2018**, *14*, 1800135.

- (44) Martinez-Boubeta, C.; Simeonidis, K.; Makridis, A.; Angelakeris, M.; Iglesias, O.; Guardia, P.; Cabot, A.; Yedra, L.; Estradé, S.; Peiró, F.; et al. Learning from Nature to Improve the Heat Generation of Iron-Oxide Nanoparticles for Magnetic Hyperthermia Applications. *Sci. Rep.* **2013**, *3*, 1–8.
- (45) Noh, S.-h.; Na, W.; Jang, J.-t.; Lee, J.-H.; Lee, E. J.; Moon, S. H.; Lim, Y.; Shin, J.-S.; Cheon, J. Nanoscale Magnetism Control via Surface and Exchange Anisotropy for Optimized Ferrimagnetic Hysteresis. *Nano Lett.* **2012**, *12*, 3716–3721.
- (46) Mohapatra, J.; Xing, M.; Liu, J. P. Inductive Thermal Effect of Ferrite Magnetic Nanoparticles. *Materials* **2019**, *12*, 3208.
- (47) Nishimoto, K.; Ota, S.; Shi, G.; Takeda, R.; Trisnanto, S. B.; Yamada, T.; Takemura, Y. High Intrinsic Loss Power of Multicore Magnetic Nanoparticles with Blood-Pooling Property for Hyperthermia. *AIP Adv.* **2019**, *9*, 035347.
- (48) Jordan, A.; Scholz, R.; Wust, P.; Fähling, H.; Felix, R. Magnetic Fluid Hyperthermia (MFH): Cancer Treatment with AC Magnetic Field Induced Excitation of Biocompatible Superparamagnetic Nanoparticles. J. Magn. Magn. Mater. 1999, 201, 413–419.
- (49) Wildeboer, R. R.; Southern, P.; Pankhurst, Q. A. On the Reliable Measurement of Specific Absorption Rates and Intrinsic Loss Parameters in Magnetic Hyperthermia Materials. *J. Phys. D: Appl. Phys.* **2014**, *47*, 495003.
- (50) Bastus, N. G.; Kogan, M. J.; Amigo, R.; Grillo-Bosch, D.; Araya, E.; Turiel, A.; Labarta, A.; Giralt, E.; Puntes, V. F. Gold Nanoparticles for Selective and Remote Heating of β -Amyloid Protein Aggregates. *Mater. Sci. Eng. C* **2007**, 27, 1236–1240.
- (51) Sanchez, C.; Diab, D. E. H.; Connord, V.; Clerc, P.; Meunier, E.; Pipy, B.; Payré, B.; Tan, R. P.; Gougeon, M.; Carrey, J.; et al. Targeting a G-Protein-Coupled Receptor Overexpressed in Endocrine Tumors by Magnetic Nanoparticles To Induce Cell Death. *ACS Nano* **2014**, *8*, 1350–1363.
- (52) Creixell, M.; Bohórquez, A. C.; Torres-Lugo, M.; Rinaldi, C. EGFR-Targeted Magnetic Nanoparticle Heaters Kill Cancer Cells without a Perceptible Temperature Rise. ACS Nano 2011, 5, 7124—7129
- (53) Villanueva, A.; de la Presa, P.; Alonso, J. M.; Rueda, T.; Martínez, A.; Crespo, P.; Morales, M. P.; Gonzalez-Fernandez, M. A.; Valdés, J.; Rivero, G. Hyperthermia HeLa Cell Treatment with Silica-Coated Manganese Oxide Nanoparticles. *J. Phys. Chem. C* **2010**, *114*, 1976—1981.
- (54) Rabin, Y. Is Intracellular Hyperthermia Superior to Extracellular Hyperthermia in the Thermal Sense? *Int. J. Hyperther.* **2009**, *18*, 194–202
- (55) Riedinger, A.; Guardia, P.; Curcio, A.; Garcia, M. A.; Cingolani, R.; Manna, L.; Pellegrino, T. Subnanometer Local Temperature Probing and Remotely Controlled Drug Release Based on Azo-Functionalized Iron Oxide Nanoparticles. *Nano Lett.* **2013**, *13*, 2399—2406.
- (56) Chen, G. Nonlocal and Nonequilibrium Heat Conduction in the Vicinity of Nanoparticles. *J. Heat Transfer* **1996**, *118*, 539–545.
- (57) Cahill, D. G.; Braun, P. v.; Chen, G.; Clarke, D. R.; Fan, S.; Goodson, K. E.; Keblinski, P.; King, W. P.; Mahan, G. D.; Majumdar, A.; et al. Nanoscale Thermal Transport. II. 2003–2012. *Appl. Phys. Rev.* 2014, 1, 011305.
- (58) Chiu-Lam, A.; Rinaldi, C. Nanoscale Thermal Phenomena in the Vicinity of Magnetic Nanoparticles in Alternating Magnetic Fields. *Adv. Funct. Mater.* **2016**, *26*, 3933–3941.
- (59) Keblinski, P.; Cahill, D. G.; Bodapati, A.; Sullivan, C. R.; Taton, T. A. Limits of Localized Heating by Electromagnetically Excited Nanoparticles. *J. Appl. Phys.* **2006**, *100*, 054305.
- (60) Goyal, H.; Vlachos, D. G. Multiscale Modeling of Microwave-Heated Multiphase Systems. *Chem. Eng. J.* **2020**, 397, 125262.
- (61) Joshi, A. A.; Majumdar, A. Transient Ballistic and Diffusive Phonon Heat Transport in Thin Films. J. Appl. Phys. 1993, 74, 31.
- (62) Dalba, G.; Fornasini, P. IUCr. EXAFS Debye—Waller Factor and Thermal Vibrations of Crystals. urn:issn:0909-0495. *J. Synchrotron Radiat* 1997, 4, 243–255.

- (63) Brezovich, I. A.; Atkinson, W. J.; Lilly, M. B. Local Hyperthermia with Interstitial Techniques. *Cancer Research* **1984**, 44, 4752s.
- (64) Comaschi, T.; Balerna, A.; Mobilio, S. Temperature Dependence of the Structural Parameters of Gold Nanoparticles Investigated with EXAFS. *Phys. Rev. B: Condens. Matter Mater. Phys.* **2008**, *77*, 075432.
- (65) Espinosa, A.; Castro, G. R.; Reguera, J.; Castellano, C.; Castillo, J.; Camarero, J.; Wilhelm, C.; García, M. A.; Muñoz-Noval, Á. Photoactivated Nanoscale Temperature Gradient Detection Using X-Ray Absorption Spectroscopy as a Direct Nanothermometry Method. *Nano Lett.* **2020**, *21*, 769–777.
- (66) Ano, T.; Tsubaki, S.; Liu, A.; Matsuhisa, M.; Fujii, S.; Motokura, K.; Chun, W.-J.; Wada, Y. Probing the Temperature of Supported Platinum Nanoparticles under Microwave Irradiation by in Situ and Operando XAFS. Commun. Chem. 2020, 3, 1–11.
- (67) Dong, J.; Zink, J. I. Taking the Temperature of the Interiors of Magnetically Heated Nanoparticles. ACS Nano 2014, 8, 5199–5207.
- (68) Brites, C. D. S.; Lima, P. P.; Silva, N. J. O.; Millán, A.; Amaral, V. S.; Palacio, F.; Carlos, L. D. Thermometry at the Nanoscale. *Nanoscale* **2012**, *4*, 4799–4829.
- (69) Zhong, J.; Liu, W.; Kong, L.; Morais, P. C. A New Approach for Highly Accurate, Remote Temperature Probing Using Magnetic Nanoparticles. *Sci. Rep.* **2014**, *4*, 1–5.
- (70) Silva, P. L.; Savchuk, O. A.; Gallo, J.; García-Hevia, L.; Bañobre-López, M.; Nieder, J. B. Mapping Intracellular Thermal Response of Cancer Cells to Magnetic Hyperthermia Treatment. *Nanoscale* **2020**, *12*, 21647–21656.
- (71) Cui, Y.; Zou, W.; Song, R.; Yu, J.; Zhang, W.; Yang, Y.; Qian, G. A Ratiometric and Colorimetric Luminescent Thermometer over a Wide Temperature Range Based on a Lanthanide Coordination Polymer. *Chem. Commun.* **2013**, *50*, 719–721.
- (72) Li, L.; Qin, F.; Zhang, Z. A Non-Invasive Luminescent Nano-Thermometer: Approaching the Maximum Thermal Sensitivity of Er³⁺ Ion's Green Emission. *CrystEngComm* **2019**, *21*, 3256–3263.
- (73) Jia, M.; Lin, F.; Sun, Z.; Fu, Z. Novel Excited-State Nanothermometry Combining the Red-Shift of Charge-Transfer Bands and a Thermal Coupling Effect. *Inorg. Chem. Front.* **2020**, *7*, 3932–3937.
- (74) Senapati, S.; Nanda, K. K. Wide-Range Thermometry at Micro/Nano Length Scales with In2O3 Octahedrons as Optical Probes. *ACS Appl. Mater. Interfaces* **2015**, *7*, 23481–23488.
- (75) Cerruti, M. G.; Sauthier, M.; Leonard, D.; Liu, D.; Duscher, G.; Feldheim, D. L.; Franzen, S. Gold and Silica-Coated Gold Nanoparticles as Thermographic Labels for DNA Detection. *Anal. Chem.* **2006**, *78*, 3282–3288.
- (76) Li, Y.; Li, B. Q. Use of CdTe Quantum Dots for High Temperature Thermal Sensing. RSC Adv. 2014, 4, 24612–24618.
- (77) Sun, T.-Y.; Zhang, D.-Q.; Yu, X.-F.; Xiang, Y.; Luo, M.; Wang, J.-H.; Tan, G.-L.; Wang, Q.-Q.; Chu, P. K. Dual-Emitting Nanocomposites Derived from Rare-Earth Compound Nanotubes for Ratiometric Fluorescence Sensing Applications. *Nanoscale* **2013**, *5*, 1629–1637.
- (78) Han, Y.; Liu, Y.; Zhao, H.; Vomiero, A.; Li, R. Highly Efficient Ratiometric Nanothermometers Based on Colloidal Carbon Quantum Dots. J. Mater. Chem. B 2021, 9, 4111–4119.
- (79) Ran, W.; Noh, H. M.; Park, S. H.; Lee, B. R.; Kim, J. H.; Jeong, J. H.; Shi, J. Er³⁺-Activated NaLaMgWO₆ Double Perovskite Phosphors and Their Bifunctional Application in Solid-State Lighting and Non-Contact Optical Thermometry. *Dalton Trans.* **2019**, 48, 4405–4412
- (80) Lojpur, V.; Antić, Ž.; Dramićanin, M. D. Temperature Sensing from the Emission Rise Times of Eu³⁺ in SrY₂O₄. *Phys. Chem. Chem. Phys.* **2014**, *16*, 25636–25641.
- (81) Aigouy, L.; Saïdi, E.; Lalouat, L.; Labéguerie-Egéa, J.; Mortier, M.; Löw, P.; Bergaud, C. AC Thermal Imaging of a Microwire with a Fluorescent Nanocrystal: Influence of the near Field on the Thermal Contrast. J. Appl. Phys. 2009, 106, 074301.

- (82) Saïdi, E.; Samson, B.; Aigouy, L.; Volz, S.; Löw, P.; Bergaud, C.; Mortier, M. Scanning Thermal Imaging by Near-Field Fluorescence Spectroscopy. *Nanotechnology* **2009**, *20*, 115703.
- (83) Ozvat, T. M.; Sterbinsky, G. E.; Campanella, A. J.; Rappé, A. K.; Zadrozny, J. M. EXAFS Investigations of Temperature-Dependent Structure in Cobalt-59 Molecular NMR Thermometers. *Dalton Trans.* **2020**, *49*, 16380–16385.
- (84) Collins, S. F.; Baxter, G. W.; Wade, S. A.; Sun, T.; Grattan, K. T. V.; Zhang, Z. Y.; Palmer, A. W. Comparison of Fluorescence-Based Temperature Sensor Schemes: Theoretical Analysis and Experimental Validation. *J. Appl. Phys.* **1998**, *84*, 4649.
- (85) Brites, C. D. S.; Balabhadra, S.; Carlos, L. D. Lanthanide-Based Thermometers: At the Cutting-Edge of Luminescence Thermometry. *Adv. Opt. Mater.* **2019**, *7*, 1801239.
- (86) Fornasini, P.; Grisenti, R. On EXAFS Debye-Waller Factor and Recent Advances. J. Synchrotron Radiat. 2015, 22, 1242–1257.
- (87) Mishra, P.; Pandey, B. K. Variation of Debye Temperature with Size of Nanoparticles. *AIP Conf. Proc.* **2020**, 2220, 020061.
- (88) Hodges, J. M.; Morse, J. R.; Williams, M. E.; Schaak, R. E. Microscopic Investigation of Chemoselectivity in Ag-Pt-Fe₃O₄ Heterotrimer Formation: Mechanistic Insights and Implications for Controlling High-Order Hybrid Nanoparticle Morphology. *J. Am. Chem. Soc.* **2015**, *137*, 15493–15500.
- (89) Luo, J.; Monai, M.; Wang, C.; Lee, J. D.; Duchoň, T.; Dvořák, F.; Matolín, V.; Murray, C. B.; Fornasiero, P.; Gorte, R. J. Unraveling the Surface State and Composition of Highly Selective Nanocrystalline Ni–Cu Alloy Catalysts for Hydrodeoxygenation of HMF. *Catal. Sci. Technol.* **2017**, *7*, 1735–1743.
- (90) Dong, A.; Ye, X.; Chen, J.; Kang, Y.; Gordon, T.; Kikkawa, J. M.; Murray, C. B. A Generalized Ligand-Exchange Strategy Enabling Sequential Surface Functionalization of Colloidal Nanocrystals. *J. Am. Chem. Soc.* **2010**, *133*, 998–1006.
- (91) Luo, J.; Yun, H.; Mironenko, A. v.; Goulas, K.; Lee, J. D.; Monai, M.; Wang, C.; Vorotnikov, V.; Murray, C. B.; Vlachos, D. G.; et al. Mechanisms for High Selectivity in the Hydrodeoxygenation of 5-Hydroxymethylfurfural over PtCo Nanocrystals. *ACS Catal.* **2016**, 6, 4095–4104.
- (92) Wang, C.; Luo, J.; Liao, V.; Lee, J. D.; Onn, T. M.; Murray, C. B.; Gorte, R. J. A Comparison of Furfural Hydrodeoxygenation over Pt-Co and Ni-Fe Catalysts at High and Low H₂ Pressures. *Catal. Today* **2018**, *302*, 73–79.
- (93) Luo, J.; Arroyo-Ramírez, L.; Wei, J.; Yun, H.; Murray, C. B.; Gorte, R. J. Comparison of HMF Hydrodeoxygenation over Different Metal Catalysts in a Continuous Flow Reactor. *Appl. Catal., A* **2015**, 508, 86–93.
- (94) Ravel, B.; Newville, M. ATHENA, ARTEMIS, HEPHAESTUS: Data Analysis for X-Ray Absorption Spectroscopy Using IFEFFIT. *J. Synchrotron Radiat.* **2005**, *12*, 537–541.
- (95) Mohapatra, J.; Zeng, F.; Elkins, K.; Xing, M.; Ghimire, M.; Yoon, S.; Mishra, S. R.; Liu, J. P. Size-Dependent Magnetic and Inductive Heating Properties of Fe₃O₄ Nanoparticles: Scaling Laws across the Superparamagnetic Size. *Phys. Chem. Chem. Phys.* **2018**, 20, 12879–12887.
- (96) Jiles, D. C.; Atherton, D. L. Theory of Ferromagnetic Hysteresis (Invited). *J. Appl. Phys.* **1984**, *55*, 2115.
- (97) Corbellini, L.; Plathier, J.; Lacroix, C.; Harnagea, C.; Ménard, D.; Pignolet, A. Hysteresis Loops Revisited: An Efficient Method to Analyze Ferroic Materials. *J. Appl. Phys.* **2016**, *120*, 124101.
- (98) Müller, K.-H. Magnetic Viscosity; Elsevier, 2016.
- (99) Serletis, C.; Efthimiadis, K. G. On the Measurement of Magnetic Viscosity. *J. Magn. Magn. Mater.* **2012**, 324, 2547–2552.
- (100) Yamamoto, Y.; Ogasawara, J.; Himukai, H.; Itoh, T. Effects of Coating Molecules on the Magnetic Heating Properties of Au-Fe₃O₄ Heterodimer Nanoparticles. *Appl. Phys. Lett.* **2016**, *109*, 142406.
- (101) Gibertini, M.; Koperski, M.; Morpurgo, A. F.; Novoselov, K. S. Magnetic 2D Materials and Heterostructures. *Nat. Nanotechnol.* **2019**, *14*, 408–419.
- (102) Kikkawa, T.; Suzuki, M.; Ramos, R.; Aguirre, M. H.; Okabayashi, J.; Uchida, K.; Lucas, I.; Anadón, A.; Kikuchi, D.;

- Algarabel, P. A.; et al. Interfacial Ferromagnetism and Atomic Structures in High-Temperature Grown Fe₃O₄/Pt/Fe₃O₄ Epitaxial Trilayers. *J. Appl. Phys.* **2019**, *126*, 143903.
- (103) Figueroa, S. J. A.; Stewart, S. J.; Rueda, T.; Hernando, A.; de la Presa, P. Thermal Evolution of Pt-Rich FePt/Fe₃O₄ Heterodimers Studied Using X-Ray Absorption Near-Edge Spectroscopy. *J. Phys. Chem. C* **2011**, *115*, 5500–5508.
- (104) Ramos, R.; Kikkawa, T.; Anadón, A.; Lucas, I.; Niizeki, T.; Uchida, K.; Algarabel, P. A.; Morellón, L.; Aguirre, M. H.; Ibarra, M. R.; et al. Interface-Induced Anomalous Nernst Effect in Fe₃O₄/Pt-Based Heterostructures. *Appl. Phys. Lett.* **2019**, *114*, 113902.
- (105) Dunand, A.; Flack, H. D.; Yvon, K. Bonding Study of TiC and TiN. I. High-Precision X-Ray-Diffraction Determination of the Valence-Electron Density Distribution, Debye-Waller Temperature Factors, and Atomic Static Displacements in span Class. *Phys. Rev. B: Condens. Matter Mater. Phys.* 1985, 31, 2299.
- (106) Zhao, Y. H.; Lu, K. Grain-Size Dependence of Thermal Properties of Nanocrystalline Elemental Selenium Studied by X-Ray Diffraction. *Phys. Rev. B: Condens. Matter Mater. Phys.* **1997**, *56*, 14330.
- (107) Eastman, J. A.; Fitzsimmons, M. R.; Thompson, L. J. The Thermal Properties of Nanocrystalline Pd from 16 to 300 K. *Phil. Mag. B* **2006**, *66*, *667*–*696*.
- (108) Kale, S. S.; Asensio, J. M.; Estrader, M.; Werner, M.; Bordet, A.; Yi, D.; Marbaix, J.; Fazzini, P.-F.; Soulantica, K.; Chaudret, B. Iron Carbide or Iron Carbide/Cobalt Nanoparticles for Magnetically-Induced CO₂ Hydrogenation over Ni/SiRAlOx Catalysts. *Catal. Sci. Technol.* **2019**, *9*, 2601–2607.
- (109) Asensio, J. M.; Miguel, A. B.; Fazzini, P. F.; van Leeuwen, P. W. N. M.; Chaudret, B. Hydrodeoxygenation Using Magnetic Induction: High -TemperatureHeterogeneous Catalysis in Solution. *Angew. Chem., Int. Ed.* **2019**, *58*, 11306–11310.
- (110) Marbaix, J.; Mille, N.; Carrey, J.; Soulantica, K.; Chaudret, B. Magnetically Induced Nanocatalysis for Intermittent Energy Storage: Review of the Current Status and Prospects. *Nanoparticles Catal.* **2021**, 307–329.
- (111) Meffre, A.; Mehdaoui, B.; Connord, V.; Carrey, J.; Fazzini, P. F.; Lachaize, S.; Respaud, M.; Chaudret, B. Complex Nano-Objects Displaying Both Magnetic and Catalytic Properties: A Proof of Concept for Magnetically Induced Heterogeneous Catalysis. *Nano Lett.* 2015, 15, 3241–3248.

